Application of discrete-element methods to approximate sea-ice dynamics

A. Damsgaard[1], A. Adcroft[1], and O. Sergienko[1]

[1]Program in Atmospheric and Oceanic Sciences, Princeton University, Princeton, New Jersey, USA

Key Points:

- Abrupt strengthening under dense ice-packing configurations induces granular jamming
- Cohesive bonds can provide similar behavior as Coulomb-frictional parameterizations
- A probabilistic model characterizes the likelihood of jamming over time

Corresponding author: A. Damsgaard, `andersd@princeton.edu`

Abstract

Lagrangian models of sea-ice dynamics have several advantages over Eulerian continuum models. Spatial discretization on the ice-floe scale as well as arbitrary concentrations are natural for Lagrangian models. This allows for improved model performance in ice-marginal zones. Furthermore, Lagrangian models can explicitly simulate jamming processes similar to sea ice movement through narrow confinements. Granular jamming is a stochastic process that occurs when the right grains arrive at the right place at the right time, and the jamming likelihood over time can be described by a probabilistic model. While difficult to parameterize in continuum formulations, jamming emerges spontaneously in dense granular systems simulated in a Lagrangian framework. Here, we present a flexible discrete-element framework for approximating Lagrangian sea-ice mechanics at the ice-floe scale, forced by ocean and atmosphere velocity fields. Our goal is to optimize the computational efficiency of mechanical ice-floe interaction relative to traditional discrete-element methods for granular dynamics. We demonstrate that frictionless contact models based on compressive stiffness alone are unlikely to produce jamming, and describe two different approaches based on Coulomb-friction and cohesion which both result in increased bulk shear strength of the granular assemblage. The frictionless but cohesive contact model can display jamming behavior which on the large scale is highly similar to the more complex model with Coulomb friction and ice-floe rotation, and is significantly simpler in computational cost.

1 Introduction

Sea ice influences the atmosphere and ocean in high latitudes and thus the state of the climate throughout the globe [e.g. *Curry et al.*, 1995; *Deser et al.*, 2000; *Chiang and Bitz*, 2005]. In climate models, large-scale behavior of sea ice is typically simulated using (elastic-)viscous-plastic [e.g. *Thorndike et al.*, 1975; *Hibler*, 1979; *Hunke and Dukowicz*, 1997] or elastic-plastic continuum models [e.g. *Weiss et al.*, 2007; *Feltham*, 2008; *Girard et al.*, 2011; *Rampal et al.*, 2016]. Observations show that sea ice deformation in shear zones exhibits anisotropic properties [e.g. *Wilchinsky and Feltham*, 2006; *Girard et al.*, 2009; *Weiss and Schulson*, 2009]. However, in continuum models shear zones are greatly affected by grid resolution and mesh orientation [e.g. *Rudnicki and Rice*, 1975; *de Borst*, 1991]. The model behavior can be improved by using non-viscous rheologies and adaptive meshes [e.g. *Girard et al.*, 2011; *Rampal et al.*, 2016]. Moreover, continuum formulations are generally not well-suited for simulating the ice-marginal zone, where spatial variability in sea-ice concentration and ice-floe thickness cause strong changes in mechanical properties. In such circumstances, continuum models can not simulate advection of a diverse ice pack correctly [e.g. *Horvat and Tziperman*, 2015].

1.1 Sea ice as a granular material

Previous studies argued that sea ice can be treated as a granular material, with a bulk rheology determined by the self-organizing complexity of discrete and interacting ice floes [e.g. *Coon*, 1974; *Bak et al.*, 1988; *Tremblay and Mysak*, 1997; *Hopkins*, 2004; *Feltham*, 2005; *Hopkins and Thorndike*, 2006]. Examples of granular phenomena include jets of sea-ice floes in the marginal-ice zone [e.g. *Feltham*, 2005], and jamming [*Samelson et al.*, 2006; *Kwok et al.*, 2010; *Herman*, 2013; *Rallabandi et al.*, 2017a,b]. Granular jamming in the sea-ice pack controls ice flux through narrow confinements such as the Nares Strait between Greenland and Canada [e.g. *Kwok et al.*, 2010; *Rallabandi et al.*, 2017a,b]. Jamming and clogging of flow through conduits is a common phenomenon in dense granular materials [e.g. *Cates et al.*, 1998; *To et al.*, 2001; *Zuriguel*, 2014]. The Beverloo method [*Beverloo et al.*, 1961] is a common approach to determine granular flux through an orifice under the influence of a constant body force. This approach assumes that grains accelerate from no motion to an equilibrium motion with the body force from some distance upstream to the orifice opening. The simplest formulations assume plug-like flow through the orifice, and the flux relations may be modified to account for friction against the orifice side. However, the Beverloo equation fails to account for granular jamming and resultant clogging, which can inhibit flow through smaller openings relative to the grain size. Granular materials have a highly non-linear shear strength as a function of packing fraction or porosity. The non-linear granular rheology can cause clogging in continuum models [e.g. *Rallabandi et al.*, 2017a,b], but does not capture the stochastic complexity associated the jamming process. A probabilistic model can describe the likelihood of granular clogging [e.g. *Tang et al.*, 2009; *Thomas and Durian*, 2015]. In the model proposed by *Tang et al.* [2009] the chance of survival P_s (the opposite of jamming) decreases exponentially with time t:

$$P_\mathrm{s} = \exp(-t/T), \tag{1}$$

where the characteristic time scale of jamming T is dependent on the material, the experimental geometry and the forcing. The Mohr-Coulomb frictional coefficient μ_u that links shear stress τ_u with compressive normal stress N controls the mechanics of dense assemblages of granular materials:

$$\tau_\mathrm{u} = C + \mu_\mathrm{u} N, \tag{2}$$

where C is the material cohesion. This relationship is well established for granular materials [e.g. *Terzaghi et al.*, 1996] and ice [*Fortt and Schulson*, 2007; *Feltham*, 2008; *Fortt and Schulson*, 2009; *Schulson and Fortt*, 2012]. The effect of inertia on the post-failure rheology is described by the magnitude of the dimensionless inertia number I:

$$I = \dot{\gamma}\bar{d}\sqrt{\frac{\rho}{N}}, \tag{3}$$

where $\dot{\gamma}$ is the shear-strain rate, $\bar{d}$ is the representative grain diameter, and ρ is the grain density. For low values of the inertia number ($I \lesssim 10^{-3}$), granular rheology is essentially rate independent, and the Mohr-Coulomb frictional coefficient μ_u and dilative response is constant [e.g. *GDR-MiDi*, 2004]. For values of $I \gtrsim 10^{-3}$, granular materials behave as viscoplastic *Bingham materials*, with the frictional coefficient depending in a nonlinear fashion on the inertia number [*GDR-MiDi*, 2004; *da Cruz et al.*, 2005; *Jop et al.*, 2006; *Forterre and Pouliquen*, 2008], i.e. $\tau_\mathrm{u} = \mu_\mathrm{u}(I)N$. In this regime, it is possible to uniquely link the stress and strain, convenient for continuum modeling approaches. However, the $\mu_\mathrm{u}(I)$-rheology does not include effects of non-locality [e.g. *Henann and Kamrin*, 2013], and, therefore, deformation is not distributed through material-dependent shear zones of finite width, in contrast to observations. The (elastic-)viscous-plastic continuum models have the same limitations (further discussions in *Rallabandi et al.* [2017a] and *Rallabandi et al.* [2017b]). Dilation represents an additional complexity to granular shear zones with rigid particles, and is induced in dense packings as grains need space for relative movement [e.g. *Reynolds*, 1885; *Nedderman*, 1992; *Terzaghi et al.*, 1996; *Tremblay and Mysak*, 1997; *Wilchinsky et al.*, 2010, 2011]. The magnitude of dilation depends on material properties and the applied forcing [e.g. *Aharonov and Sparks*, 2002; *Damsgaard et al.*, 2013].

1.2 Numerical methods for granular materials

The discrete-element method (DEM, also known as the *distinct element method*) is widely used to model granular media and discontinuous materials in a variety of contexts [e.g. *Radjaï and Dubois*, 2011]. The most popular approach is the *soft-body* DEM, originally derived from molecular-dynamics modeling principles by *Cundall and Strack* [1979], where grain kinematics are determined by explicit temporal integration of their momentum balance. The DEM has been applied with discretizations on the sub-ice floe scale [*Hopkins et al.*, 1991], or with particles representing a collection of ice floes [*Li et al.*, 2014]. Thus far, for sea-ice modeling the DEM is typically applied to simulate one ice floe per particle [e.g. *Gutfraind and Savage*, 1997; *Hopkins*, 2004; *Herman*, 2016].

However, the DEM and other Lagrangian approaches to modeling sea-ice dynamics have not been used as components of global climate models, primarily because of computational considerations. Sea-ice models based on smoothed-particle hydrodynamics (SPH) have been proposed [e.g. *Gutfraind and Savage*, 1998; *Lindsay and Stern*, 2004], which offer better computational performance and Lagrangian discretizations. However, the complexity and kinematic phase transitions of granular materials are notoriously difficult to generalize in continuum formulations required for Eulerian models and SPH approaches.

The DEM is generally a computationally intensive approach. Due to the Lagrangian nature of the method, sophisticated neighbor-search algorithms are required to minimize the computational cost of contact mapping. Furthermore, the explicit temporal integration of the per-grain momentum balance is determined by the seismic wave propagation through the granular assemblage, and thus requires short time steps for attaining numerical stability [e.g. *Kruggel-Emden et al.*, 2008; *Radjaï and Dubois*, 2011],

$$\Delta t \leq \frac{\epsilon}{\sqrt{\frac{\max(k_\mathrm{n})}{\min(m)}}}, \tag{4}$$

where ϵ is a safety factor (e.g. $\epsilon = 0.07$), $\max(k_\mathrm{n})$ is the largest elastic stiffness in the system, and $\min(m)$ is the smallest particle mass. As apparent from Eq. 4 small ice floes heavily penalize the time step length, while softening of the elastic modulus can speed up the computations. In order to increase the computational efficiency, it is common in DEM applications to both truncate smaller grain sizes and reduce the elastic stiffness of the grains, which increases the time step. The effect of these modifications can be assessed by evaluating the inertia number (Eq. 3). If it remains in the rate-independent regime of $I \lesssim 10^{-3}$, a grain-size increase and/or elastic softening will be inconsequential for the overall strength and dilative behavior of the granular system.

The goal of this study is to develop a numerical approach for simulating sea ice on the individual floe scale, which, at the same time, is computationally efficient to be used as a component of a climate model [e.g. *Griffies et al.*, 2005; *Delworth et al.*, 2006; *Gnanadesikan et al.*, 2006]. To do so, we make methodological simplifications relative to other discrete-element studies on sea ice, and explore the large-scale implications of different choices of contact rheology.

2 Methods

2.1 Governing equations

For computational efficiency, we treat the ice floes as cylinders moving in two dimensions along the atmosphere-ocean interface. Their geometry is described by thickness h and horizontal radius r. The translational momentum balance for an ice floe with index i is:

$$m^i \frac{D^2 \boldsymbol{x}^i}{Dt^2} = \underbrace{\sum_j \left(\boldsymbol{f}_\text{n}^{ij} + \boldsymbol{f}_\text{t}^{ij} \right)}_{\text{Contact forces}} + \boldsymbol{f}_\text{o}^i + \boldsymbol{f}_\text{a}^i, \tag{5}$$

where m is the ice-floe mass, $\boldsymbol{x}$ is ice-floe center position, and $\boldsymbol{f}_\text{n}$ and $\boldsymbol{f}_\text{t}$ is granular contact-normal and tangential force from interaction with ice floe j. The external forces $\boldsymbol{f}_\text{o}$ and $\boldsymbol{f}_\text{a}$ are ocean and atmosphere-induced drag, respectively. Similarly, the angular momentum balance for grain i is:

$$J_z^i \frac{D^2 \Omega^i}{Dt^2} = \underbrace{\sum_j \left(r^i \boldsymbol{n}^{ij} \times \boldsymbol{f}_\text{t}^{ij} \right)}_{\text{Contact torques}} + t_\text{o}^i + t_\text{a}^i. \tag{6}$$

J_z is the moment of inertia around the vertical center axis, and Ω is the angular position of ice floe i. The ocean and atmosphere can induce rotational torques t_o and t_a due to floe vorticity or ice-floe rotation. The respective forces and torques that appear in the linear and angular momentum balances are described below. In this study, and in the above equations for momentum, we disregard Coriolis forces, sea-surface slope, or wave action. These simplifications are due to the idealized nature of our simulation setups. We integrate the momentum-balance equations in time using a third-order Taylor expansion scheme, which is computationally simple and has a high level of numerical precision [e.g. *Kruggel-Emden et al.*, 2008].

The presented experiments compare the jamming behavior of two differing ice-floe contact models. Common to both models, the resistive force $\boldsymbol{f}_\text{n}$ to axial compressive strain between to cylindrical ice floes i and j is provided by (Hookean) linear elasticity, based on the overlap distance δ_n. This is a common approach in discrete-element simulations [e.g. *Cundall and Strack*, 1979; *Luding*, 2008; *Ergenzinger et al.*, 2011; *Damsgaard* *et al.*, 2016, 2017]:

$$\boldsymbol{f}_{\mathrm{n}}^{ij} = A^{ij} E^{ij} \boldsymbol{\delta}_{\mathrm{n}}^{ij} \quad \text{when} \quad 0 > |\boldsymbol{\delta}_{\mathrm{n}}^{ij}| \equiv |\boldsymbol{x}^i - \boldsymbol{x}^j| - (r^i + r^j). \tag{7}$$

The contact cross-sectional area $A^{ij} = R^{ij} \min(h^i, h^j)$ is determined by the harmonic mean $R^{ij} = 2r^i r^j/(r^i + r^j)$ of the ice-floe radii r^i and r^j, as well as the smallest of the involved ice-floe thicknesses h^i and h^j. The harmonic mean of Young's modulus E^{ij} scales the linear-elastic force resulting from axial strain of a distance $|\boldsymbol{\delta}_{\mathrm{n}}^{ij}|$. The stiffness is scale invariant [e.g. *Obermayr et al.*, 2013], and assumes constant elastic properties of the ice itself, regardless of ice-floe size. We note that nonlinear elasticity models based on Hertzian contact mechanics may alternatively be applied to determine the stresses resulting from contact compression [e.g. *Herman*, 2013, 2016]. However, with nonlinear stiffness models the numerical stability of the explicit temporal integration scheme depends on the stress and packing state of the granular assemblage, and will under compressive-stress extremes require very small time steps. In the above model, we use a Young's modulus of $E = 2.0 \times 10^7$ Pa which strikes a reasonable balance between elastic compressibility and computational efficiency.

As we demonstrate below, models based on compressive strength alone result in a weak sea-ice pack, and are not sufficient to cause granular clogging. We explore two modifications to the contact model presented in Eq. 7. The first approach is typical to DEM models and is based on resolving shear resistance through tangential (contact parallel) elasticity, not exceeding the Coulomb frictional limit. An alternative approach, fundamentally complementary to compressive elasticity and shear friction, is tensile strength of ice-floe contacts which leads to a cohesive bulk granular rheology.

2.2 Tangential elasticity with Coulomb friction

DEM models typically include resistance against slip between particles, by limiting relative tangential movement for inter-particle contacts [e.g. *Cundall and Strack*, 1979]. Tangential elasticity is resolved by determining the contact transverse travel distance $\boldsymbol{\delta}_{\mathrm{t}}$ (i.e. the vector of shear motion) on the contact plane for the duration of the contact t_{c}:

$$\boldsymbol{\delta}_{\mathrm{t}}^{ij} = \int_0^{t_{\mathrm{c}}} \left[(\boldsymbol{v}^i - \boldsymbol{v}^j) \cdot \hat{\boldsymbol{t}}^{ij} - R^{ij} \left(\omega^i + \omega^j \right) \right], \tag{8}$$

where $\boldsymbol{v}$ and ω denotes linear and angular velocity, respectively. The contact-parallel unit vector is denoted $\hat{\boldsymbol{t}}$. The contact transverse travel distance $\boldsymbol{\delta}_{\mathrm{t}}$ is corrected for contact rotation over the duration of the interaction, and is used to determine the contact-tangential elastic force:

$$\boldsymbol{f}_{\mathrm{t}}^{ij} = \frac{E^{ij} A^{ij}}{R^{ij}} \frac{2(1-(\nu^{ij})^2)}{(2-\nu^{ij})(1+\nu^{ij})} \boldsymbol{\delta}_{\mathrm{t}}^{ij}, \tag{9}$$

with ν^{ij} is the harmonic mean of the Poisson's ratios set for the ice floes. We use a constant value of $\nu = 0.185$ [*Hopkins*, 2004]. Coulomb friction on the grain surface limits the tangential force, relative to the magnitude of the normal force:

$$|\boldsymbol{f}_{\mathrm{t}}^{ij}| \leq \mu^{ij} |\boldsymbol{f}_{\mathrm{n}}^{ij}|. \tag{10}$$

The Coulomb-frictional coefficient μ introduced above describes resistance to sliding along the individual *grain surfaces*, and should not be mistaken for the *bulk* Mohr-Coulomb frictional coefficient μ_{u} (Eq. 2) that describes frictional behavior of an assemblage of many grains. In the case of slip ($|\boldsymbol{f}_{\mathrm{t}}| > \mu |\boldsymbol{f}_{\mathrm{n}}|$) the length of the contact transverse travel distance $\boldsymbol{\delta}_{\mathrm{t}}$ reduces to be consistent with the Coulomb limit. This loss in energy storage accounts for tangential contact plasticity and irreversible work associated with contact sliding. Since the above model of tangential shear resistance is based on deformation distance on the inter-floe contact plane, it requires solving for ice-floe rotational kinematics of each ice floe and a bookkeeping algorithm for storing contact histories.

2.3 Tensile contact strength

Cohesion (mechanical attraction between ice floes) is introduced by parameterizing resistance to extension beyond the overlap distance between a pair of ice floes (i.e. $\delta_{\mathrm{n}}^{ij} > 0$). For actual ice floes, tensile strength arises due to refreezing processes at the ice-floe interface or due to mechanical ridging. The general description of bond deformation includes resistance to bond tension, shear, twist, and rolling [e.g. *Potyondy and Cundall*, 2004; *Obermayr et al.*, 2013; *Herman*, 2016]. However, for this study we explore the possibility of using bond *tension* alone as a mechanical component contributing to bulk granular shear strength.

We parameterize tensile strength by applying Eq. 7 for the extensive regime ($\delta_{\mathrm{n}} > 0$). Eq. 7 is enforced until the tensile stress exceeds the tensile strength σ_{c} defined for the bonds:

$$|\mathbf{f}_{\mathrm{n}}^{ij}| \leq \min(\sigma_{\mathrm{c}}^{i}, \sigma_{\mathrm{c}}^{j}) A^{ij}. \tag{11}$$

Cross-sectional area of the contact is found as $A^{ij} = R^{ij} \min(h^i, h^j)$ as in Eq. 7. We set the bonds to obtain full tensile strength as soon as a pair of ice floes first undergo compression ($\delta_n < 0$). Time-dependent strengthening ($\sigma_c(t)$ and $d\sigma_c/dt > 0$) causes a strain-rate weakening that is not of immediate interest for this study.

2.4 Drag from ocean and atmosphere

We adapt v^2-type parameterizations for characterizing Stokes drag forces between ice floes and ocean or atmosphere. This approach is common in both Lagrangian and Eulerian models [e.g. *Hopkins*, 2004; *Herman*, 2016; *Rallabandi et al.*, 2017a],

$$\boldsymbol{f}_\mathrm{o}^i = \pi \rho_\mathrm{o} \left(c_{\mathrm{v,o}} 2 r^i D^i + c_{\mathrm{h,o}} (r^i)^2 \right) (\boldsymbol{v}_\mathrm{o} - \boldsymbol{v}^i) |\boldsymbol{v}_\mathrm{o} - \boldsymbol{v}^i|, \tag{12}$$

where we use an idealized value of $\rho_\mathrm{o} = 1 \times 10^3$ kg m^{-3} as ocean density, D is the ice-floe draft (here set to $D^i = 9h^i/10$), and $c_{\mathrm{v,o}} = 0.14$ and $c_{\mathrm{h,o}} = 1.6 \times 10^{-4}$ are vertical and horizontal drag coefficients. The ocean velocity is $\boldsymbol{v}_\mathrm{o}$ and ice-floe velocity is $\boldsymbol{v}$. Similarly, for the atmosphere-induced drag:

$$\boldsymbol{f}_\mathrm{a}^i = \pi \rho_\mathrm{a} \left(c_{\mathrm{v,a}} 2 r^i (h^i - D^i) + c_{\mathrm{h,a}} (r^i)^2 \right) (\boldsymbol{v}_\mathrm{a} - \boldsymbol{v}^i) |\boldsymbol{v}_\mathrm{a} - \boldsymbol{v}^i|. \tag{13}$$

The atmosphere density is $\rho_\mathrm{a} = 1.3$ kg m^{-3}. The vertical and horizontal drag coefficients are $c_{\mathrm{v,a}} = 0.064$ and $c_{\mathrm{h,a}} = 8.0 \times 10^{-5}$, respectively. The wind velocity is $\boldsymbol{v}_\mathrm{a}$. The curl of the ocean or atmosphere velocities ($\nabla \times \boldsymbol{v}_\mathrm{f}$) induces a rotational torque (t) on the ice floes [e.g. *Nakayama and Boucher*, 1998], sometimes ignored in DEM sea-ice models:

$$t_\mathrm{o}^i = \pi (r^i)^4 \rho_\mathrm{o} \left(\frac{r^i}{5} c_{\mathrm{h,o}} + D^i c_{\mathrm{v,o}} \right) ((\nabla \times \boldsymbol{v}_\mathrm{o})/2 - \omega^i) |(\nabla \times \boldsymbol{v}_\mathrm{o})/2 - \omega^i|, \tag{14}$$

and

$$t_\mathrm{a}^i = \pi (r^i)^4 \rho_\mathrm{o} \left(\frac{r^i}{5} c_{\mathrm{h,a}} + (h^i - D^i) c_{\mathrm{v,a}} \right) ((\nabla \times \boldsymbol{v}_\mathrm{a})/2 - \omega^i) |(\nabla \times \boldsymbol{v}_\mathrm{a})/2 - \omega^i|, \tag{15}$$

where ω is the ice-floe angular velocity. The above terms add rotational drag for a spinning ice floe, and can induce rotation for ice floes in ocean or atmosphere fields with high vorticity. Ocean and atmosphere curl may be reasonable to neglect on the ice-floe scale [e.g. *Herman*, 2016], but are included here nonetheless.

2.5 Boundary conditions

The domain boundaries can interact with the granular assemblage in a variety of ways. Ice floes are disabled from mechanical interaction with the rest of the ice floes when crossing an *inactive boundary*. Ice floes can interact mechanically across opposite sides of the model domain if the edges are *periodic boundaries*, and are immediately repositioned to the opposite side if they cross a domain edge. *Fixed boundaries* are created by placing ice floes along a line and keeping them fixed in space. Optionally, the fixed grains can move at prescribed velocities. Finally, flat and frictionless walls can provide *normal stress boundaries* to the granular assemblage. These walls attempt to fulfill a certain contact stress normal to their geometric orientation, and move through time to uphold the prescribed stress. They are assigned a constant mass, and their kinematics are resolved with explicit temporal integration of their stress balance, similar to the temporal integration performed for the ice floes themselves.

2.6 Model limitations

The presented model is not sufficiently general for being a complete formulation for sea-ice mechanics. For example, we do not include a parameterization of pressure ridging, important for mechanical redistribution of ice mass in converging regimes [e.g. *Thorndike et al.*, 1975; *Rothrock*, 1975; *Hibler*, 1980; *Hopkins et al.*, 1991; *Flato and Hibler*, 1995; *Lipscomb et al.*, 2007]. Furthermore, the ice floe shape is highly simplified as we neglect geometrical anisotropy and associated mechanical effects [e.g. *Hopkins*, 2004; *Wilchinsky and Feltham*, 2006; *Feltham*, 2008; *Wilchinsky et al.*, 2011]. However, direct modeling of polygonal sea-ice floes is computationally excessive in the targeted context. Here we focus on differences between simple DEM models with the fewest additional layers of abstraction. Consequentially, the simulation results should not be compared directly to real settings, as further analysis and model development is required to do so.

3 Numerical model

3.1 Implementation

The model described above is implemented as a stand-alone DEM sea-ice model that uses drag from prescribed ocean and atmosphere velocity fields. When the sea-ice model is used as a component of a climate model, the drag forces are computed by the ocean and atmospheric model components, respectively, and passed to the sea-ice component. In this study, the stand-alone and purpose-built DEM model `Granular.jl` [*Damsgaard*, 2018a] is used to explore strengths and limitations of different methods related to sea-ice mechanics. A separate online repository contains the simulation scripts [*Damsgaard*, 2018b].

The effects of the ocean and atmosphere are here prescribed as constant velocity fields. The interpolation to the discrete ice floes is determined with bilinear interpolation and conformal mapping, allowing for non-orthogonal cells in the ocean and atmosphere grids. Ice-floe contacts are detected by binning the population of ice floes with in a grid, where the cell width equals the largest ice floe diameter. All contacts for an ice floe can reliably be detected by searching for overlaps within the current and eight neighboring cells. Ice floes are transferred between the cell lists according to their movement through the sorting grid. This approach significantly reduces the computational overhead ($O(n)$) compared to all-to-all contact searches ($O(n^2)$) [e.g. *Ericson*, 2005]. We do not include thermodynamic processes and ice-floe geometries do not change over the course of each simulation.

3.2 Experiments

We perform two types of experiments in order to understand the granular rheology and its applicability to simulate sea-ice dynamics. In both cases we generate ice-floe sizes by a power-law distribution within the range $r_{\min}$ to $r_{\max}$ with an exponent of value -1.8, commonly used for describing sea ice in the marginal zone [e.g. *Steer et al.*, 2008; *Herman*, 2010, 2013]. For the experiments we parameterize the granular interaction in one of two ways:

1. **Coulomb-frictional DEM**: Linear-elastic resistance to compressive strain normal to the contact interface (Eq. 7) and linear-elastic resistance to shear strain on the contact interface, with Coulomb friction limiting the tangential force magnitude (Eq. 10). The kinematics are resolved with the translational and rotational momentum equations (Eqs. 5 and 6).
2. **Cohesive DEM**: Linear-elastic resistance to compressive strain normal to the contact interface (Eq. 7) and linear-elastic resistance to extensional strain between a bonded ice-floe pair with a breakage criterion (Eq. 11). The kinematics are resolved for translation only (Eq. 5). Rotation (Eq. 6) and contributing components (Eqs. 8, 9, 10, and 14–15) are ignored.

Approach (1) requires that rotational kinematics of the ice floes are resolved (Eq. 6) for correctly determining the tangential contact displacement (Eq. 8). Including rotation approximately doubles the kinematic degrees of freedom and required computations. Approach (2) is computationally cheaper as it does not require resolving rotation (the ice floes are effectively frictionless). Instead, shear strength is for the dense granular system contributed by the topology and the cohesive contact network. The Coulomb-frictional model (approach 1) is the standard method for simulating cohesionless granular materials, and will for our purposes serve as a benchmark for testing the applicability of the less complex cohesive model (approach 2).

3.2.1 Simple shear

We perform simple shear experiments on dense granular packings, where the ice floes are sheared from a pre-consolidated state under a constant normal stress (Fig. 1). The primary objective of these experiments is to validate the Mohr-Coulomb frictional behavior typical for granular materials (Eq. 2) [e.g. *Nedderman*, 1992], and assess how the type of grain-to-grain contact rheology influences bulk stress properties. In the shear experiments we do not include ocean and atmosphere drag, as we are interested in analyzing the ice-floe mechanics alone.

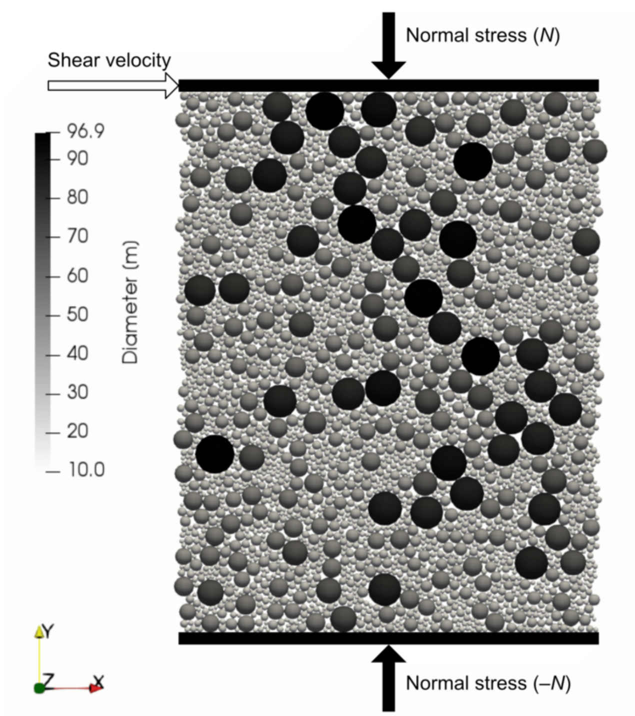

Figure 1. Simulation setup for the simple shear experiments. The upper and lower walls exert a prescribed normal stress to the granular assemblage, and a constant velocity along x is enforced for the uppermost ice floes. Left and right ($-x$ and $+x$) boundaries are periodic.

We adapt a simple-shear setup with boundary conditions typical in DEM modeling [e.g. *Damsgaard et al.*, 2013], with a schematic overview in Figure 1. We initially generate ice floes with radii between 5 and 50 m in an irregular spatial arrangement without geometrical overlaps. We then apply a uniform ocean drag towards the lower boundary ($-y$) in order to increase the packing ratio. We then disable the ocean drag and perform a *consolidation step* in order to further uniaxially compress the packing in equilibrium with the stress forcing, as common in Mohr-Coulomb tests on granular materials [e.g. *Bowles*, 1992; *Mitchell and Soga*, 2005]. The consolidation is performed by adding a normal stress boundary condition to the top ($+y$). Finally, we perform a constant-rate *shear step* by prescribing a velocity towards $+x$ of 1 m s^{-1} to the grains just below the upper boundary (Fig. 1). The bulk shear stress is determined from the sum of contact forces along y against the top grains. The side boundaries ($-x$ and $+x$) are periodic in order allow arbitrary shear strains without geometrical constraints. Grains at the lower boundary ($-y$) are fixed in space in order to provide geometrical and mechanical roughness. The parameter choices result in granular inertia parameters in the range of $I = [10^{-3}; 10^{-2}]$ (Eq. 3), so slight shear-rate dependence on the observed bulk shear stress can be expected.

3.2.2 Jamming in idealized straits

In this set of experiments we use ocean and atmosphere drag to push the ice floes through a confining strait of funnel-shaped geometry (Fig. 2), and analyze how the ice-floe properties influences the likelihood of granular jamming. The geometry is similar to ones from earlier studies focused on ice-discharge with smoothed particle dynamics and a discrete element model outside of the regime of granular jamming [*Gutfraind and Savage*, 1998]. The ice floes are forced with wind and ocean current fields oriented from north to south. The spatial velocity pattern of the ocean is defined by a stream function, where the ocean flows through the confining strait with a velocity field consistent with mass conservation. Ice floes are initially placed in a pseudo-random arrangement north of the channel. During our initial tests we observed that the simulated material never jammed *inside* the flat-walled channel, but always at or before the channel entrance. For that reason, we constrain our simulation domain size to only include the relevant parts.

New ice floes are continuously added to the top of the domain as soon as there is space to accommodate them. The sizes are drawn from the same power-law size distribution. The bottom edge of the domain is an inactive boundary. Over the cause of each

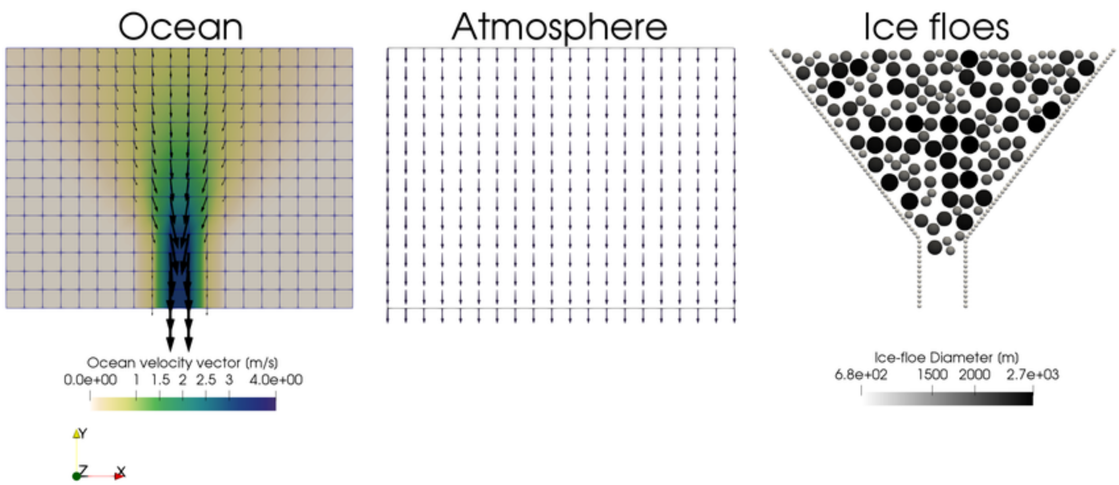

Figure 2. Simulation setup for the idealized strait experiments. Ocean velocities vary from 0 to 4 m/s relative to the bounding geometry, while the atmosphere velocity field is a uniform value of 30 m/s.

experiment we determine the mass of disabled ice floes at the bottom as a measure of cumulative ice transport through the strait. If granular jamming occurs, ice floes stop reaching the bottom. We impose the criteria that the ice mass at the bottom must have been constant for more than one hour in simulation time for being classified as jammed. The experiments rely on pseudo-random number generation (pRNG) for generating ice-floe size distributions, in order to obtain statistical description of the behavior (Eq. 1). The radii are drawn between 600 and 1350 m. We seed the pRNG with different values and repeat each experiment ten times with identical mechanical parameters to assess the statistical probability of granular jamming.

4 Results

In the following we compare bulk behavior between the algorithmically complex Coulomb-frictional model and the simpler cohesive model. The supplementary material contains animations of the shear and jamming experiments.

4.1 Simple shear

We observe that both the Coulomb-frictional and cohesive models follow the Mohr-Coulomb constitutive relation (Eq. 2), as the bulk shear stress of the granular assemblages τ_u scales linearly with normal stress N applied normal to the shear direction (Fig. 3a).

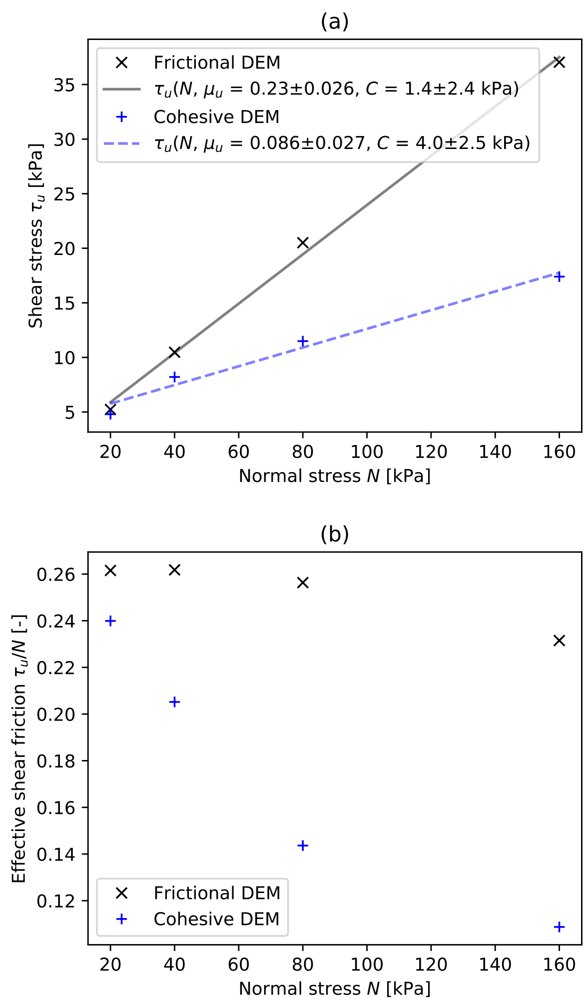

Figure 3. Steady-state stress and friction during simple shear for Coulomb-frictional model runs (μ = 0.3 and σ_c = 0 kPa, see Eq. 10 and 11), and cohesive model runs (μ = 0 and σ_c = 200 kPa). (a) The bulk shear stress τ_u increases linearly with the applied normal stress. We optimize Eq. 2 using a least-squares fit and note parameter estimates and 95% confidence intervals in the legend. (b) Effective friction observed in the two model types.

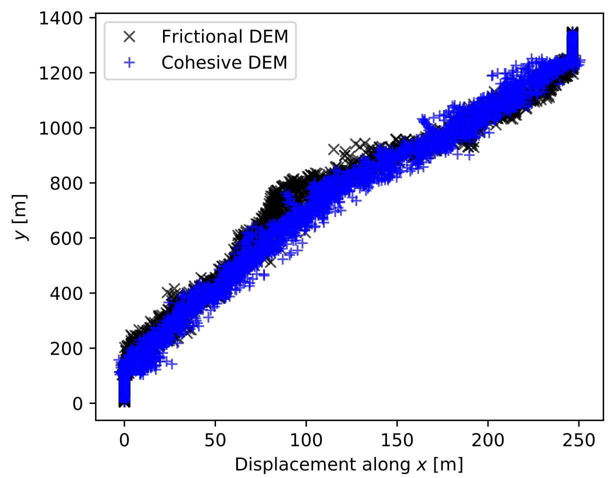

Figure 4. Ice-floe displacements in the simple shear experiments with a normal stress of N = 20 kPa.

The Coulomb-frictional model produces an ice-floe pack with a small value for bulk cohesion (C) and a strong linear correlation between normal stress and shear stress. The cohesive model results in an ice-floe pack with a higher bulk cohesion, but it also shows increasing shear stresses with increasing normal stress. A metric that describes stress bulk properties is the effective shear friction (τ_u/N), a ratio between observed bulk shear stress and applied normal stress. We determine the values from the shear experiments (Fig. 3b). For the Coulomb-frictional tests, we see that the bulk frictional coefficient ($\mu_u \approx 0.23$, Eq. 2) is lower than the Coulomb-frictional coefficient we parameterize on the contact level ($\mu = 0.3$, Eq. 10). Ice-floe rotation decreases the bulk strength, which is common for two-dimensional granular systems with circular grains. The Coulomb-frictional model retains most of its effective friction under the tested range of normal stresses, in line with observations of sea ice mechanics. In contrast, the cohesive model becomes monotonically weaker under larger normal stresses. The distribution of shear strain (Fig. 4) is similar in the two models. The only difference is that shear strain is slightly more localized towards the moving boundary in the Coulomb-frictional DEM, and more linear and distributed in the cohesive DEM.

4.2 Jamming in idealized straits

By adjusting the grain-to-grain frictional coefficient μ (Eq. 10) and the tensile strength σ_c (Eq. 11) we can assess jamming tendencies in the two models. Figure 6 shows that

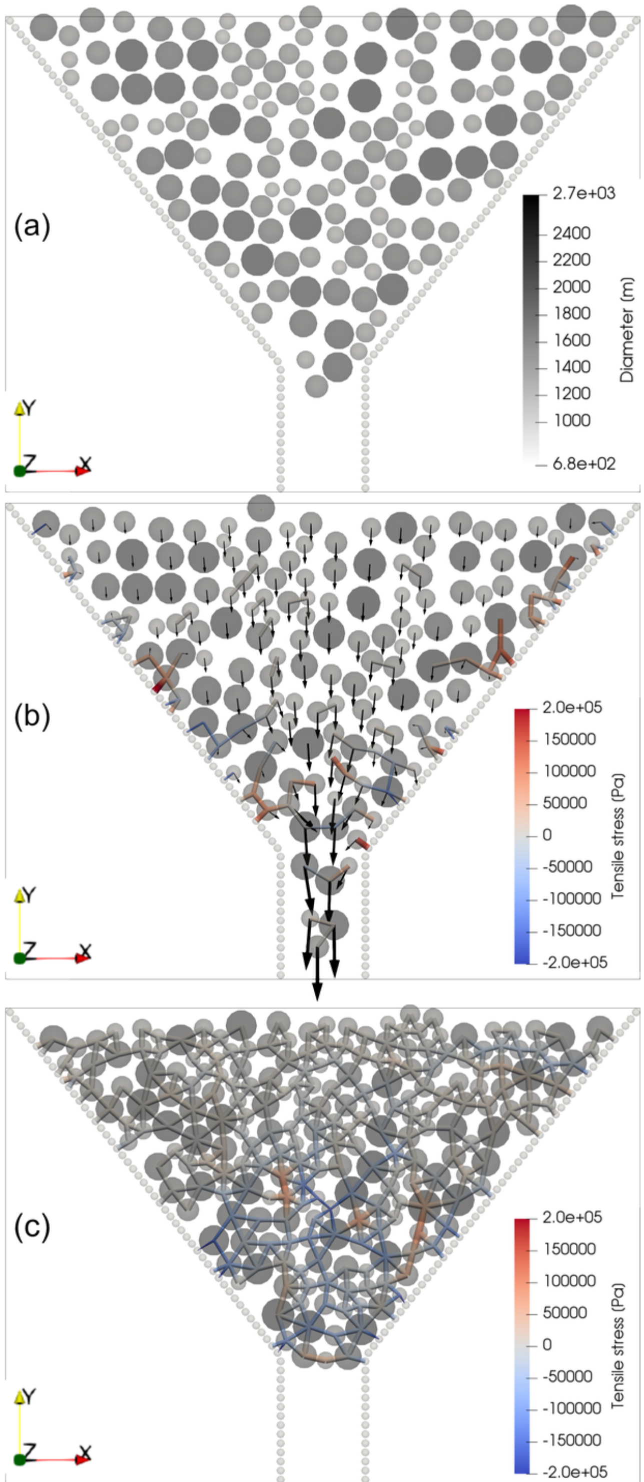

Figure 5. Example visualization of the granular system for the *idealized strait* runs, here the initial state (a), during flow (b), and in a jammed state (c). Black arrows denote the linear velocity of the ice floes, and colored bars indicate compressive or tensile granular interactions. The above visualizations are for run one out of ten with $\mu = 0$ and $\sigma_c = 400$ kPa.

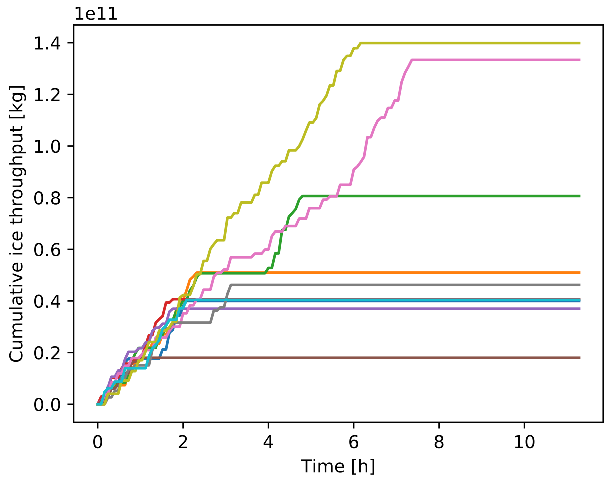

Figure 6. The cumulative mass of ice flushed through the idealized strait over time in experiments of identical mechanical parameters (cohesive model, $\mu = 0$ and $\sigma_c = 400$ kPa), but with random perturbations to the initial ice-floe placements and sizes.

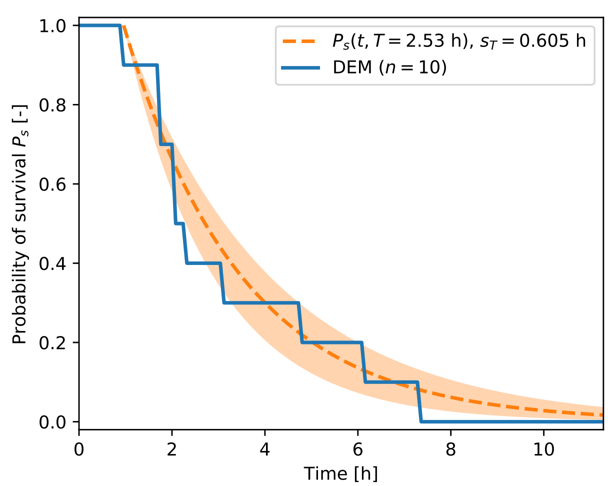

Figure 7. Probability of survival (non-jamming) P_s for the ensemble in Fig. 6, with a corresponding least-square fit of Eq. 1. The legend shows the best-fit value for the characteristic jamming time T, as well as the sample standard deviation around the mean.

the jamming is a stochastic process. With the applied contact parameters ($\mu = 0$ and $\sigma_c = 400$ kPa), all ten runs jam after a period of ~7 hours. We plot the ratio of survived (non-jammed) runs as a function of time (Fig. 7), and fit an exponential decay function to the survival fraction [Eq. 1, *Tang et al.*, 2009] with the Levenberg-Marquardt algorithm of nonlinear least squares optimization. The decay time-scale parameter T and the sample standard deviation s_T are useful metrics for comparing the effect of different prescribed properties to the jamming behavior of the ice-pack system. We offset the curve fit in time corresponding to the first occurrence of jamming.

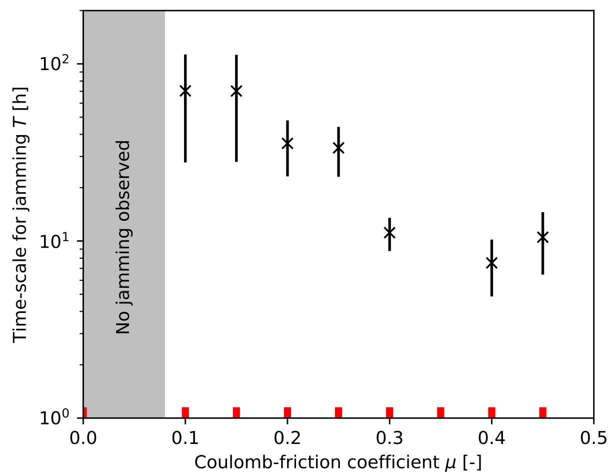

Figure 8. The influence of the Coulomb-frictional coefficient μ (Eq. 10) on the characteristic time for jamming T (Eq. 1) through a strait of width $W = 6000$ m. Red ticks denote tested values. A statistically significant fit could not be achieved from the ensemble with $\mu = 0.35$.

We observe that larger friction coefficients μ increase the mechanical rigidity and increase the likelihood of jamming in the Coulomb-frictional model with rotation (Fig. 8). Similarly, increases in grain-to-grain tensile strength increases the likelihood of jamming in the reduced-complexity model with cohesion (Fig. 9). Neither model displays jamming as the system becomes frictionless ($\mu \to 0$) or cohesionless ($\sigma_c \to 0$), highlighting the need for including interactions other than contact-normal elastic repulsion (Eq. 7). Furthermore, a unique value for tensile strength σ_c can be found corresponding to the jamming behavior of a certain Coulomb-frictional coefficient μ. We then compare jamming behavior of the Coulomb-frictional model ($\mu = 0.3$ and $\sigma_c = 0$ kPa) and the cohesive

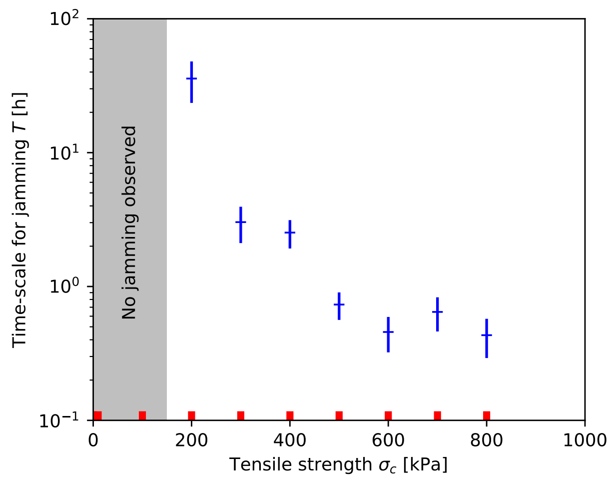

Figure 9. The influence of the tensile strength σ_c (Eq. 11) on the characteristic time for jamming T (Eq. 1) through a strait of width W = 6000 m. Red ticks denote tested values.

model (μ = 0 and σ_c = 200 kPa), which show jamming characteristics with time scales of the same order of magnitude (Fig. 8 and 9).

In both models, jamming does not occur across wide straits, consistent with the expectation of constant granular discharge across wide confinements (Fig. 10). As strait width decreases, the jamming timescale T decreases in a nonlinear fashion for both the Coulomb-frictional and cohesive models. With the applied parameters the Coulomb-frictional model was able to jam in straits of width W = 7000 m, while the cohesive model only displayed jamming up to W = 6000 m.

We also increase the width of the generated particle-size distribution (PSD) around the same mean value, and observe that jamming occurs faster in wide size spans (Fig. 11). While smaller ice floes act as lubricants facilitating flow, larger ice floes provide structural rigidity leading to eventual jamming. It is primarily the advection of larger ice floes to the strait entrance that cause the jamming itself. In the Coulomb-frictional model, ice-floe thickness does not directly influence jamming behavior (Fig. 12), as the presented implementation adjusts stress-based yield criteria for contact sliding and tensile bond breakage accordingly. However, the cohesive model displays increased jamming with larger thicknesses, corresponding to our expectations of the system behavior.

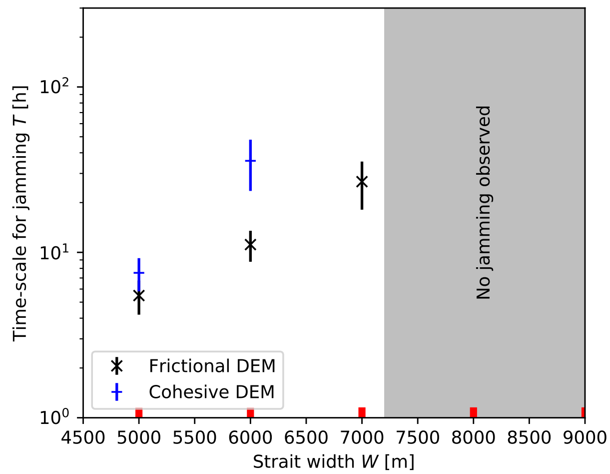

427 **Figure 10.** Jamming behavior with increasing width of the strait (Fig. 5) for Coulomb-frictional (μ = 0.3
428 and σ_c = 0 kPa) and cohesive runs (μ = 0 and σ_c = 200 kPa).

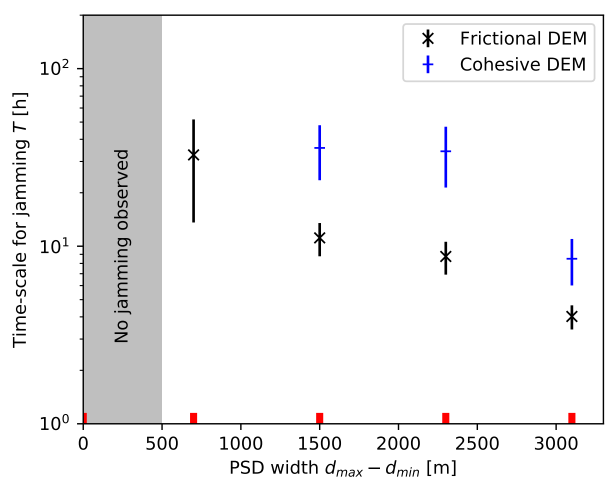

444 **Figure 11.** Jamming behavior with increasing width of the particle-size distribution for Coulomb-frictional
445 (μ = 0.3 and σ_c = 0 kPa) and cohesive runs (μ = 0 and σ_c = 200 kPa). Red ticks denote tested values.

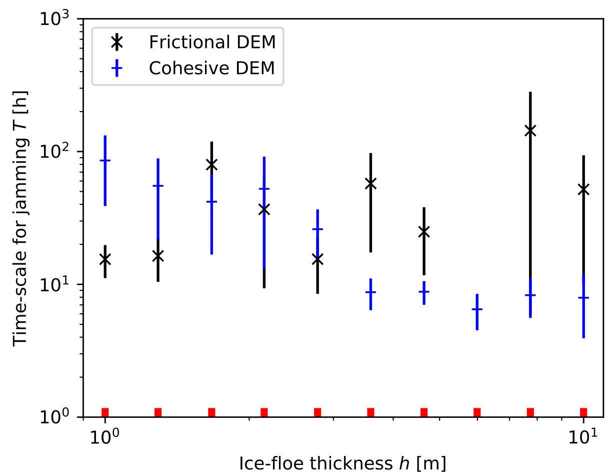

Figure 12. Jamming behavior with uniformly increasing thickness of the ice floes for Coulomb-frictional (μ = 0.3 and σ_c = 0 kPa) and cohesive runs (μ = 0 and σ_c = 200 kPa). Red ticks denote tested values.

5 Discussion and Summary

We construct a flexible discrete-element framework for simulating Lagrangian sea-ice dynamics at the ice-floe scale, forced by ocean and atmosphere velocity fields. While frictionless contact models based on tensile stiffness alone are very unlikely to jam, we describe two different approaches based on Coulomb friction and tensile strength. Both additions result in increased bulk shear strength of the granular assemblage. We demonstrate that the discrete-element approach is able to undergo granular jamming when forced through an idealized confinement, where the probability of jamming is determined by the channel width, ice-floe thicknesses, and ice-floe size variability. The frictionless but cohesive contact model can with certain tensile strength values display jamming behavior which on the large scale is broadly similar to a model with contact friction and ice-floe rotation.

We note that our results are consistent with previous studies on granular mechanics, specifically regarding how the magnitude of the Coulomb-frictional coefficient influences bulk behavior. *Morgan* [1999] demonstrated that the particle-frictional coefficient increases bulk frictional strength of dense and two-dimensional systems up to a certain point where grain rolling becomes dominant over grain-to-grain contact sliding. *Kamrin and Koval* [2014] showed that particle-surface friction effects bulk behavior, and that increasing Coulomb-frictional coefficients increase shear strength. Furthermore, and under certain conditions, the spatial distribution of shear deformation can be affected by the micromechanical grain friction. *Morgan* [2015] investigated the combined effects of Coulomb friction and tensile cohesion on the structural and mechanical evolution of fold and thrust belts and contractional wedges. In this formation, broken bonds did not reform over time. It was observed that large tensile bond strengths caused increases in bulk shear strength, primarily by increasing the bulk cohesion in the Mohr-Coulomb constitutive relationship. Cohesion caused the material to behave in a rigid manner, with thin shear zones of broken bonds where bonds have failed. Without cohesion, deformation was more distributed in space. In our experiments, we observe similar behavior where increasing tensile strengths makes a dense ice pack behave like a rigid system (Fig. 5c). However, our parameterization reforms bonds progressively when ice floes again come into contact, which limits the strain weakening otherwise associated with bond breaking.

The Coulomb-frictional DEM model naturally strengthens in a linear manner with increasing compressive stress on the contacts (Eq. 10), which linearly increases bulk shear strength (Fig. 3a), as typical for granular materials tested in laboratory shear devices or when simulated with the DEM [e.g. *Damsgaard et al.*, 2013; *Morgan*, 2015]. The contacts of the cohesive model do not strengthen due to increased contact loading, which explains the weaker behavior observed at large normal stresses (Fig. 3c). However, shear strength does still increase, since larger normal stresses on the shear zone cause self-arrangement into a denser packing. The dense system contains relatively more contacts containing tensile strength, which on a bulk scale strengthens the mechanical resistance to shear. The shear profiles are not significantly different between the two profiles (Fig. 4), so we do not expect notable difference in deformation patterns on larger scales.

The method presented in this study contains many simplifications relative to sea ice in nature, both in terms of geometry and interaction. There is comfortable room for improvements if computational efficiency is less than a central concern. Cylindrical or circular grain-shape representations slightly reduce bulk shear strength relative to particles of irregular shape [e.g. *Mair et al.*, 2002]. In an attempt to compensate for shape-induced weakening, the Coulomb-frictional coefficient or tensile strength can be increased in order to tend to the desired bulk mechanics. Furthermore, it may be beneficial to add random variation to mechanical properties (e.g., μ and σ_c), if the range of variability is well understood. Ice-floe ridging is by crude means approximated by the bonding process described here, but it may be possible to improve the floe-scale mechanics for this process [e.g. *Rothrock*, 1975; *Flato and Hibler*, 1995; *Lipscomb et al.*, 2007], especially if thermodynamic balance and the important process of refreezing is determined in conjunction with ocean and atmosphere state. Instead of attempting the impossible goal of including the entire details of the complex sea-ice system, we intend for this parameterization to be a useful first attempt at making Lagrangian and ice-floe scale methods available for coupled and global climate models. Lagrangian formulations have inherent advantages to continuum sea-ice models, especially for handling the discontinuous behavior in shear zones and granular phenomena in the ice-marginal zone. We demonstrate that simplifications in discrete-element method formulations can reduce the algorithmic complexity while retaining similar shear zone morphology and jamming behavior.

Acknowledgments

We acknowledge the funding from ExxonMobil for this project. Anders Damsgaard benefited from discussions with Alon A. Stern, Mitchell Bushuk, Michael Winton, and Behrooz Ferdowsi in preparation for this paper.

References

Aharonov, E., and D. Sparks (2002), Shear profiles and localization in simulations of granular shear, *Phys. Rev., E*, *65*, 051,302.

Bak, P., C. Tang, and K. Wiesenfeld (1988), Self-organized criticality, *Phys. Rev. A*, *38*(1), 364–374, doi:10.1103/physreva.38.364.

Beverloo, W. A., H. A. Leniger, and J. van de Velde (1961), The flow of granular solids through orifices, *Chem. Eng. Sci.*, *15*(3-4), 260–269, doi:10.1016/0009-2509(61)85030-6.

Bowles, J. E. (1992), *Engineering Properties of Soils and Their Measurement*, 241 pp., Irwin/McGraw-Hill.

Cates, M. E., J. P. Wittmer, J.-P. Bouchaud, and P. Claudin (1998), Jamming, force chains, and fragile matter, *Phys. Rev. Lett.*, *81*(9), 1841–1844, doi:10.1103/physrevlett.81.1841.

Chiang, J. C. H., and C. M. Bitz (2005), Influence of high latitude ice cover on the marine Intertropical Convergence Zone, *Clim. Dyn.*, *25*(5), 477–496, doi:10.1007/s00382-005-0040-5.

Coon, M. (1974), Mechanical behavior of compacted Arctic ice floes, *J. Petr. Tech.*, *26*(04), 466–470, doi:10.2118/3956-pa.

Cundall, P. A., and O. D. L. Strack (1979), A discrete numerical model for granular assemblies, *Géotechnique*, *29*, 47–65, doi:10.1680/geot.1979.29.1.47.

Curry, J. A., J. L. Schramm, and E. E. Ebert (1995), Sea ice-albedo climate feedback mechanism, *J. Climate*, *8*(2), 240–247, doi:10.1175/1520-0442(1995)008<0240:siacfm>2.0.co;2.

da Cruz, F., S. Emam, M. Prochnow, J.-N. Roux, and F. Chevoir (2005), Rheophysics of dense granular materials: Discrete simulation of plane shear flows, *Phys. Rev. E*, *72*(2), doi:10.1103/physreve.72.021309.

Damsgaard, A. (2018a), Granular.jl: Julia package for granular dynamics simulation, Version 0.3.2, doi:10.5281/zenodo.1165990.

Damsgaard, A. (2018b), SeaIce-experiments: Simulation scripts using Granular.jl, Version 1.0.0, doi:10.5281/zenodo.1166005.

Damsgaard, A., D. L. Egholm, J. A. Piotrowski, S. Tulaczyk, N. K. Larsen, and K. Tylmann (2013), Discrete element modeling of subglacial sediment deformation, *J. Geophys. Res. Earth Surf.*, *118*, 2230–2242, doi:10.1002/2013JF002830.

Damsgaard, A., D. L. Egholm, L. H. Beem, S. Tulaczyk, N. K. Larsen, J. A. Piotrowski, and M. R. Siegfried (2016), Ice flow dynamics forced by water pressure variations in subglacial granular beds, *Geophys. Res. Lett.*, *43*, doi:10.1002/2016gl071579.

Damsgaard, A., A. Cabrales-Vargas, J. Suckale, and L. Goren (2017), The coupled dynamics of meltwater percolation and granular deformation in the sediment layer underlying parts of the big ice sheets, in *Poromechanics VI*, Am. Soc. Civ. Eng., doi:10.1061/9780784480779.024.

de Borst, R. (1991), Numerical modelling of bifurcation and localisation in cohesive-frictional materials, *Pure Appl. Geophys.*, *137*(4), 367–390.

Delworth, T. L., A. J. Broccoli, A. Rosati, R. J. Stouffer, V. Balaji, J. A. Beesley, W. F. Cooke, K. W. Dixon, J. Dunne, K. Dunne, et al. (2006), GFDL's CM2 global coupled climate models. part I: Formulation and simulation characteristics, *J. Climate*, *19*(5), 643–674.

Deser, C., J. E. Walsh, and M. S. Timlin (2000), Arctic sea ice variability in the context of recent atmospheric circulation trends, *J. Climate*, *13*(3), 617–633, doi:10.1175/1520-0442(2000)013<0617:asivit>2.0.co;2.

Ergenzinger, C., R. Seifried, and P. Eberhard (2011), A discrete element model to describe failure of strong rock in uniaxial compression, *Granul. Matter*, *13*, 341–364, doi:

10.1007/s10035-010-0230-7.

Ericson, C. (2005), *Real-Time Collision Detection*, 413–426 pp., Morgan Kaufmann/Elsevier, San Diego, CA, doi:10.1016/b978-1-55860-732-3.50015-2.

Feltham, D. L. (2005), Granular flow in the marginal ice zone, *Phil. Trans. R. Soc. A*, *363*(1832), 1677–1700, doi:10.1098/rsta.2005.1601.

Feltham, D. L. (2008), Sea ice rheology, *Ann. Rev. Fluid Mech.*, *40*(1), 91–112, doi:10.1146/annurev.fluid.40.111406.102151.

Flato, G. M., and W. D. Hibler (1995), Ridging and strength in modeling the thickness distribution of Arctic sea ice, *J. Geophys. Res.*, *100*(C9), 18,611, doi:10.1029/95jc02091.

Forterre, Y., and O. Pouliquen (2008), Flows of dense granular media, *Ann. Rev. Fluid Mech.*, *40*(1), 1–24, doi:10.1146/annurev.fluid.40.111406.102142.

Fortt, A. L., and E. M. Schulson (2007), The resistance to sliding along coulombic shear faults in ice, *Acta Mat.*, *55*(7), 2253–2264, doi:10.1016/j.actamat.2006.11.022.

Fortt, A. L., and E. M. Schulson (2009), Velocity-dependent friction on coulombic shear faults in ice, *Acta Mat.*, *57*(15), 4382–4390, doi:10.1016/j.actamat.2009.06.001.

GDR-MiDi (2004), On dense granular flows, *Eur. Phys. J. E*, *14*, 341–365, doi:10.1140/epje/i2003-10153-0.

Girard, L., J. Weiss, J. M. Molines, B. Barnier, and S. Bouillon (2009), Evaluation of high-resolution sea ice models on the basis of statistical and scaling properties of Arctic sea ice drift and deformation, *J. Geophys. Res.*, *114*(C8), doi:10.1029/2008jc005182.

Girard, L., S. Bouillon, J. Weiss, D. Amitrano, T. Fichefet, and V. Legat (2011), A new modeling framework for sea-ice mechanics based on elasto-brittle rheology, *Ann. Glaciol.*, *52*(57), 123–132, doi:10.3189/172756411795931499.

Gnanadesikan, A., K. W. Dixon, S. M. Griffies, V. Balaji, M. Barreiro, J. A. Beesley, W. F. Cooke, T. L. Delworth, R. Gerdes, M. J. Harrison, I. M. Held, W. J. Hurlin, H.-C. Lee, Z. Liang, G. Nong, R. C. Pacanowski, A. Rosati, J. Russell, B. L. Samuels, Q. Song, M. J. Spelman, R. J. Stouffer, C. O. Sweeney, G. Vecchi, M. Winton, A. T. Wittenberg, F. Zeng, R. Zhang, and J. P. Dunne (2006), GFDL's CM2 global coupled climate models. part II: The baseline ocean simulation, *J. Climate*, *19*(5), 675–697, doi:10.1175/jcli3630.1.

Griffies, S. M., A. Gnanadesikan, K. W. Dixon, J. P. Dunne, R. Gerdes, M. J. Harrison, A. Rosati, J. L. Russell, B. L. Samuels, M. J. Spelman, M. Winton, and R. Zhang (2005), Formulation of an ocean model for global climate simulations, *Ocean Sci.*, *1*(1), 45–79, doi:10.5194/os-1-45-2005.

Gutfraind, R., and S. B. Savage (1997), Marginal ice zone rheology: Comparison of results from continuum-plastic models and discrete-particle simulations, *J. Geophys. Res.: Oceans*, *102*(C6), 12,647–12,661, doi:10.1029/97jc00124.

Gutfraind, R., and S. B. Savage (1998), Flow of fractured ice through wedge-shaped channels: smoothed particle hydrodynamics and discrete-element simulations, *Mech. Mat.*, *29*(1), 1–17, doi:10.1016/s0167-6636(97)00072-0.

Henann, D. L., and K. Kamrin (2013), A predictive, size-dependent continuum model for dense granular flows, *Proc. Nat. Acad. Sci.*, *110*(17), 6730–6735, doi:10.1073/pnas.1219153110.

Herman, A. (2010), Sea-ice floe-size distribution in the context of spontaneous scaling emergence in stochastic systems, *Phys. Rev. E*, *81*(6), doi:10.1103/physreve.81.066123.

Herman, A. (2013), Shear-jamming in two-dimensional granular materials with power-law grain-size distribution, *Entropy*, *15*(11), 4802–4821, doi:10.3390/e15114802.

Herman, A. (2016), Discrete-element bonded-particle sea ice model DESIgn, version 1.3a – model description and implementation, *Geosci. Mod. Dev.*, *9*(3), 1219–1241, doi:10.5194/gmd-9-1219-2016.

Hibler, W. D. (1979), A dynamic thermodynamic sea ice model, *J. Phys. Oceanogr.*, *9*(4), 815–846, doi:10.1175/1520-0485(1979)009<0815:adtsim>2.0.co;2.

Hibler, W. D. (1980), Modeling a variable thickness sea ice cover, *Mon. Weather Rev.*, *108*(12), 1943–1973, doi:10.1175/1520-0493(1980)108<1943:mavtsi>2.0.co;2.

Hopkins, M. A. (2004), A discrete element Lagrangian sea ice model, *Eng. Comput.*, *21*(2/3/4), 409–421, doi:10.1108/02644400410519857.

Hopkins, M. A., and A. S. Thorndike (2006), Floe formation in arctic sea ice, *J. Geophys. Res.*, *111*(C11), doi:10.1029/2005jc003352.

Hopkins, M. A., W. D. Hibler, and G. M. Flato (1991), On the numerical simulation of the sea ice ridging process, *J. Geophys. Res.*, *96*(C3), 4809, doi:10.1029/90jc02375.

Horvat, C., and E. Tziperman (2015), A prognostic model of the sea-ice floe size and thickness distribution, *Cryosphere*, *9*, 2119–2134, doi:10.5194/tc-9-2119-2015.

Hunke, E. C., and J. K. Dukowicz (1997), An elastic–viscous–plastic model for sea ice dynamics, *J. Phys. Oceanogr.*, *27*(9), 1849–1867, doi:10.1175/1520-0485(1997)027<1849:aevpmf>2.0.co;2.

Jop, P., Y. Forterre, and O. Pouliquen (2006), A constitutive law for dense granular flows, *Nature*, *441*(7094), 727–730, doi:10.1038/nature04801.

Kamrin, K., and G. Koval (2014), Effect of particle surface friction on nonlocal constitutive behavior of flowing granular media, *Comput. Part. Mech.*, *1*(2), 169–176, doi:10.1007/s40571-014-0018-3.

Kruggel-Emden, H., M. Sturm, S. Wirtz, and V. Scherer (2008), Selection of an appropriate time integration scheme for the discrete element method (dem), *Comput. Chem. Eng.*, *32*(10), 2263–2279.

Kwok, R., L. T. Pedersen, P. Gudmandsen, and S. S. Pang (2010), Large sea ice outflow into the Nares Strait in 2007, *Geophys. Res. Lett.*, *37*(3), n/a–n/a, doi:10.1029/2009gl041872.

Li, B., H. Li, Y. Liu, A. Wang, and S. Ji (2014), A modified discrete element model for sea ice dynamics, *Acta Oceanol. Sin.*, *33*(1), 56–63, doi:10.1007/s13131-014-0428-3.

Lindsay, R. W., and H. L. Stern (2004), A new lagrangian model of Arctic sea ice, *J. Phys. Oceanography*, *34*(1), 272–283, doi:10.1175/1520-0485(2004)034<0272:anlmoa>2.0.co;2.

Lipscomb, W. H., E. C. Hunke, W. Maslowski, and J. Jakacki (2007), Ridging, strength, and stability in high-resolution sea ice models, *J. Geophys. Res.*, *112*(C3), doi:10.1029/2005jc003355.

Luding, S. (2008), Introduction to discrete element methods: basic of contact force models and how to perform the micro-macro transition to continuum theory, *Eur. J. Env. Civ. Eng.*, *12*(7-8), 785–826.

Mair, K., K. M. Frye, and C. Marone (2002), Influence of grain characteristics on the friction of granular shear zones, *J. Geophys. Res. Solid Earth*, *107*(B10), ECV–4.

Mitchell, J. K., and K. Soga (2005), *Fundamentals of Soil Behavior*, Wiley New York.

Morgan, J. K. (1999), Numerical simulations of granular shear zones using the distinct element method 2. Effects of particle size distribution and interparticle friction on mechanical behavior, *J. Geophys. Res.*, *104*(B2), 2721–2732.

Morgan, J. K. (2015), Effects of cohesion on the structural and mechanical evolution of fold and thrust belts and contractional wedges: Discrete element simulations, *J. Geophys. Res.: Solid Earth*, *120*(5), 3870–3896, doi:10.1002/2014jb011455.

Nakayama, Y., and R. F. Boucher (1998), *Introduction to Fluid Mechanics*, Elsevier, doi:10.1016/b978-034067649-3/50003-8.

Nedderman, R. M. (1992), *Statics and Kinematics of Granular Materials*, Cambridge University Press, Cambridge.

Obermayr, M., K. Dressler, C. Vrettos, and P. Eberhard (2013), A bonded-particle model for cemented sand, *Comput. Geotech.*, *49*, 299–313, doi:10.1016/j.compgeo.2012.09.001.

Potyondy, D. O., and P. A. Cundall (2004), A bonded-particle model for rock, *Int. J. Rock Mech. Min.*, *41*(8), 1329–1364.

Radjaï, F., and F. Dubois (2011), *Discrete-Element Modeling of Granular Materials*, 425 pp., Wiley-Iste.

Rallabandi, B., Z. Zheng, M. Winton, and H. A. Stone (2017a), Wind-driven formation of ice bridges in straits, *Phys. Rev. Lett.*, *118*(12), doi:10.1103/physrevlett.118.128701.

Rallabandi, B., Z. Zheng, M. Winton, and H. A. Stone (2017b), Formation of sea ice bridges in narrow straits in response to wind and water stresses, *J. Geophys. Res.: Oceans*, *122*(7), 5588–5610, doi:10.1002/2017jc012822.

Rampal, P., S. Bouillon, E. Ólason, and M. Morlighem (2016), neXtSIM: a new Lagrangian sea ice model, *Cryosphere*, *10*(3), 1055–1073, doi:10.5194/tc-10-1055-2016.

Reynolds, O. (1885), On the dilatancy of media composed of rigid particles in contact, *Philos. Mag.*, *20*(5), 46.

Rothrock, D. A. (1975), The energetics of the plastic deformation of pack ice by ridging, *J. Geophys. Res.*, *80*(33), 4514–4519, doi:10.1029/jc080i033p04514.

Rudnicki, J. W., and J. R. Rice (1975), Conditions for the localization of deformation in pressure-sensitive dilatant materials, *J. Mech. Phys. Solids*, *23*(6), 371–394.

Samelson, R. M., T. Agnew, H. Melling, and A. MÃijnchow (2006), Evidence for atmospheric control of sea-ice motion through Nares Strait, *Geophys. Res. Lett.*, *33*(2), doi:10.1029/2005gl025016.

Schulson, E. M., and A. L. Fortt (2012), Friction of ice on ice, *J. Geophys. Res.*, *117*(B12), doi:10.1029/2012jb009219.

Steer, A., A. Worby, and P. Heil (2008), Observed changes in sea-ice floe size distribution during early summer in the western weddell sea, *Deep Sea Res. Part II: Top. Stud. Oceanogr.*, *55*(8-9), 933–942, doi:10.1016/j.dsr2.2007.12.016.

Tang, J., S. Sagdiphour, and R. P. Behringer (2009), Jamming and flow in 2d hoppers, in *AIP Conf. Proc.*, AIP, doi:10.1063/1.3179975.

Terzaghi, K., R. B. Peck, and G. Mesri (1996), *Soil Mechanics in Engineering Practice*, John Wiley & Sons.

Thomas, C. C., and D. J. Durian (2015), Fraction of clogging configurations sampled by granular hopper flow, *Phys. Rev. Lett.*, *114*(17), doi:10.1103/physrevlett.114.178001.

Thorndike, A. S., D. A. Rothrock, G. A. Maykut, and R. Colony (1975), The thickness distribution of sea ice, *J. Geophys. Res.*, *80*(33), 4501–4513, doi: 10.1029/jc080i033p04501.

To, K., P.-Y. Lai, and H. K. Pak (2001), Jamming of granular flow in a two-dimensional hopper, *Phys. Rev. Lett.*, *86*(1), 71–74, doi:10.1103/physrevlett.86.71.

Tremblay, L.-B., and L. A. Mysak (1997), Modeling sea ice as a granular material, including the dilatancy effect, *J. Phys. Oceanogr.*, *27*(11), 2342–2360, doi:10.1175/1520-0485(1997)027<2342:msiaag>2.0.co;2.

Weiss, J., and E. M. Schulson (2009), Coulombic faulting from the grain scale to the geophysical scale: lessons from ice, *J. Phys. D: Appl. Phys.*, *42*(21), 214,017, doi: 10.1088/0022-3727/42/21/214017.

Weiss, J., E. M. Schulson, and H. L. Stern (2007), Sea ice rheology from in-situ, satellite and laboratory observations: Fracture and friction, *Earth Planet. Sci. Lett.*, *255*(1-2), 1–8, doi:10.1016/j.epsl.2006.11.033.

Wilchinsky, A. V., and D. L. Feltham (2006), Modelling the rheology of sea ice as a collection of diamond-shaped floes, *J. Non-Newton. Fluid Mech.*, *138*(1), 22–32, doi: 10.1016/j.jnnfm.2006.05.001.

Wilchinsky, A. V., D. L. Feltham, and M. A. Hopkins (2010), Effect of shear rupture on aggregate scale formation in sea ice, *J. Geophys. Res.*, *115*(C10), doi: 10.1029/2009jc006043.

Wilchinsky, A. V., D. L. Feltham, and M. A. Hopkins (2011), Modelling the reorientation of sea-ice faults as the wind changes direction, *Ann. Glaciol.*, *52*(57), 83–90, doi: 10.3189/172756411795931831.

Zuriguel, I. (2014), Invited review: Clogging of granular materials in bottlenecks, *Pap. Phys.*, *6*(0), doi:10.4279/pip.060014.